# MAX-DOAS Measurements of Tropospheric NO$_2$ and HCHO Vertical Profiles at the Longfengshan Regional Background Station in Northeastern China

Shuyin Liu [1], Siyang Cheng [1,2,*], Jianzhong Ma [1], Xiaobin Xu [1], Jinguang Lv [2], Junli Jin [3], Junrang Guo [1], Dajiang Yu [4] and Xin Dai [4]

[1] State Key Laboratory of Severe Weather & Institute of Tibetan Plateau Meteorology, Chinese Academy of Meteorological Sciences, Beijing 100081, China

[2] State Key Laboratory of Applied Optics, Changchun Institute of Optics, Fine Mechanics and Physics, Chinese Academy of Sciences, Changchun 130033, China

[3] Meteorological Observation Center of China Meteorological Administration, Beijing 100081, China

[4] Longfengshan Regional Background Station, Heilongjiang Meteorological Bureau, Wuchang 150200, China

*   Correspondence: sycheng@cma.gov.cn

**Abstract:** The vertical profiles of nitrogen dioxide (NO$_2$) and formaldehyde (HCHO) in the troposphere at the Longfengshan (LFS) regional atmospheric background station (127°36′ E, 44°44′ N, 330.5 m above sea level) from 24 October 2020 to 13 October 2021 were retrieved from solar scattering spectra by multi-axis differential optical absorption spectroscopy (MAX-DOAS). We analyzed the temporal variations of NO$_2$ and HCHO as well as the sensitivity of ozone (O$_3$) production to the concentration ratio of HCHO to NO$_2$. The largest NO$_2$ volume mixing ratios (VMRs) occur in the near-surface layer for each month, with high values concentrated in the morning and evening. HCHO has an elevated layer around the altitude of 1.4 km consistently. The means $\pm$ standard deviations of vertical column densities (VCDs) and near-surface VMRs were $4.69 \pm 3.72 \times 10^{15}$ molecule·cm$^{-2}$ and $1.22 \pm 1.09$ ppb for NO$_2$, and they were $1.19 \pm 8.35 \times 10^{16}$ molecule·cm$^{-2}$ and $2.41 \pm 3.26$ ppb for HCHO. The VCDs and near-surface VMRs for NO$_2$ were high in the cold months and low in the warm months, while HCHO presented the opposite. The larger near-surface NO$_2$ VMRs appeared in the condition associated with lower temperature and higher humidity, but this relationship was not found between HCHO and temperature. We also found the O$_3$ production at the Longfengshan station was mainly in the NO$_x$-limited regime. This is the first study presenting the vertical distributions of NO$_2$ and HCHO in the regional background atmosphere of northeastern China, which are significant to enhancing the understanding of background atmospheric chemistry and regional ozone pollution processes.

**Keywords:** NO$_2$; HCHO; vertical profile; MAX-DOAS; regional atmospheric background station

## 1. Introduction

Tropospheric nitrogen dioxide (NO$_2$) and formaldehyde (HCHO) are two important trace gases [1]. NO$_2$ is not only an important air pollutant of photochemical smog and nitric acid rain [1,2], but also one of the precursors of ozone (O$_3$), secondary aerosols, and peroxyacetyl nitrate (PAN) [1]. NO$_2$ is produced by natural processes (such as lighting and ammonia oxidation [3]) and anthropogenic emission (such as transportation [4], heating/power generation [5] and coal mining [6]). Moreover, nitrogen oxides (NO$_x$) production are closely related to the conditions of internal combustion [7]. NO$_2$ is chemically removed by photolysis and reactions with various types of free radicals or O$_3$ [2]. As the most abundant carbonyl compound in the troposphere, HCHO comes from the combustion of fossil fuels and biomass and the chemical oxidation of volatile organic compounds

(VOCs) in the atmosphere [8]. Atmospheric HCHO can be removed by various photochemical reactions [9–11]. $NO_2$ and HCHO are usually treated as proxies for nitrogen oxides ($NO_x$) and VOCs, respectively, to investigate the sensitivity of $O_3$ production [12,13].

Tropospheric columns of $NO_2$ and HCHO can be measured by satellite remote sensing, such as by the Tropospheric Monitoring Instrument (TROPOMI) [14]. Although TROPOMI has high spatial resolution ($5.5 \times 3.5$ km$^2$ at nadir), there are still large uncertainties of retrieved tropospheric $NO_2$ and HCHO in the background regions over mountain terrains [15]. For surface $NO_2$ and HCHO, there are a few methods to achieve their measurements, such as Fourier transform infrared spectroscopy (FTIR) [16] and long-range active differential optical absorption spectroscopy for $NO_2$ [17]. However, the column or surface measurements without the information of $NO_2$ and HCHO vertical distributions have limitations in understanding the spatio–temporal variations of $NO_2$ and HCHO, which are significant to the investigation of the mechanisms of atmospheric chemistry in regional pollution.

Multi-axis differential optical absorption spectroscopy (MAX-DOAS), a passive ground-based remote sensing observation technique, can be used to measure the vertical column densities (VCDs) and profiles of trace gases in the troposphere [18,19]. It is characterized by high sensitivity, fast response, simple operation, and low operating cost [20]. As early as 2001, MAX-DOAS was used to measure the $NO_2$ emissions on highways [21]. Since then, a large number of studies on MAX-DOAS have been conducted in many countries [22]. In recent years, tropospheric vertical profiles of trace gases were successfully achieved by using MAX-DOAS [23]. In the past decade, many studies on $NO_2$ and HCHO observed by ground-based MAX-DOAS have been reported in China [24–29]. These studies were mainly concentrated in urban and severely polluted areas with large populations and developed economies, such as Beijing–Tianjin–Hebei, Yangtze River Delta, Pearl River Delta, and Sichuan-Chongqing [30–34]. Under the framework of World Meteorological Organization Global Atmosphere Watch (WMO/GAW) in China, MAX-DOAS observations were performed at the background stations of Shangdianzi in the North China Plain and Waliguan in the Tibetan Plateau, revealing the levels and temporal variations of $NO_2$ and HCHO in the background atmosphere of the regions [35,36]. However, to our knowledge, no investigation on levels and temporal variations of $NO_2$ and HCHO vertical distributions has been made at a background site in the northeastern China, which limits our understanding of the photochemistry and regional pollution formation mechanisms of ozone in this area.

In this study, we performed MAX-DOAS observations at the Longfengshan regional atmospheric background station from October 2020 to October 2021 in order to enhance our understanding of the characteristics of temporal evolutions of $NO_2$ and HCHO vertical distribution in the background atmosphere. Section 2 introduces the site and instrument as well as the methods of spectral analysis and profile retrieval of $NO_2$ and HCHO. Section 3 presents the temporal variations of $NO_2$ and HCHO vertical profiles as well as the sensitivities of $O_3$ production to the ratio of HCHO to $NO_2$. Finally, the discussion and conclusions are given in Sections 4 and 5, respectively.

## 2. Experiments and Methods

### 2.1. Site and Instrument

Ground-based MAX-DOAS measurements were performed at the Longfengshan (LFS) regional atmospheric background station (127°36′ E, 44°44′ N, 330.5 m a.s.l.) from 24 October 2020 to 13 October 2021 (with a break from 10 December 2020 to 3 March 2021 due to instrument malfunction). At present, the LFS station is the only background station under the framework of the WMO/GAW in the Northeast China [37]. The atmospheric observations started in 1991 at LFS [38], which represents the background atmospheric condition in the Northeast Plain region. The LFS station is located on the west side of Longfengshan reservoir, 60 km to the southeast of Wuchang City and 185 km to the southeast of Harbin City (Figure 1). It is located at the intersection of the Songnen plain

and the Zhangguangcai ridge of the Changbai mountains. On the western side of the LFS station is the plain area, and on the eastern side is the mountainous forest area [39,40]. There are no villages in the range of 2 km away from the site, no high-density population, and no significant industrial emission sources in the range of 30 km away from the site [41].
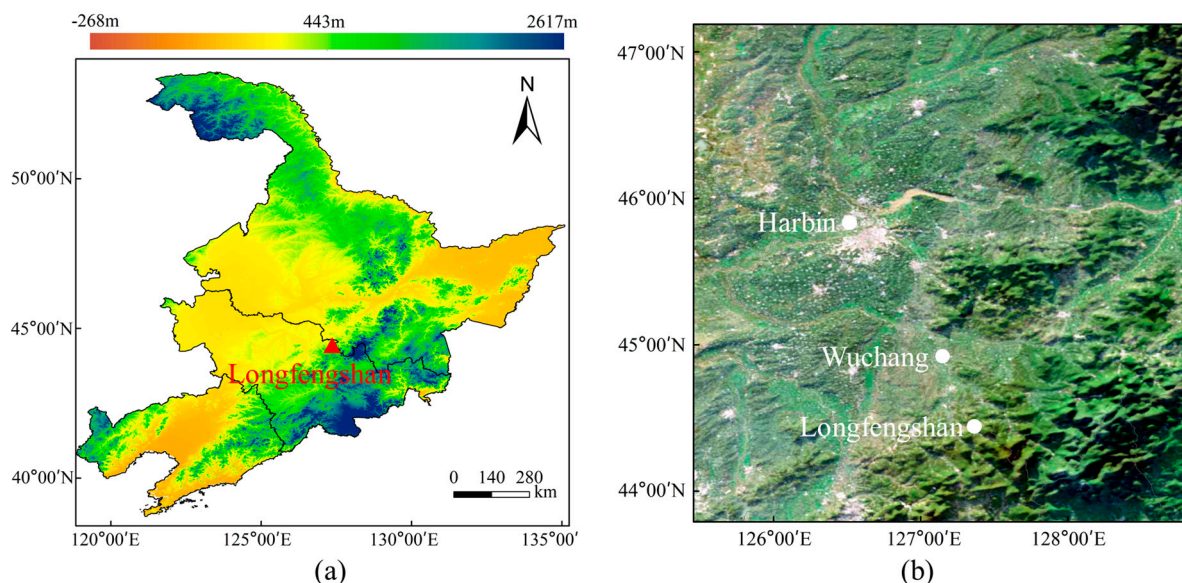


**Figure 1.** (**a**) The elevation map of Longfengshan regional atmospheric background station. (**b**) The major neighborhood cities around the LFS station (the background image is from the Sentinel−2 satellite).

We used a mini MAX-DOAS instrument from the Hoffmann Messtechnik GmbH, Germany, which was also used in our previous studies [24,36]. During the Second Cabauw Intercomparison Campaign for Nitrogen Dioxide Measuring Instruments (CINDI-2), the mean relative differences in the slant column from the reference value for the Mini MAX-DOAS were −2.10% for $NO_2$ and −20.70% for HCHO [42]. The observation system consisted of an indoor section and an outdoor section. The outdoor section contains the entrance optics, fiber-coupled spectrograph, and controlling electronics inside a metal box. A stepper motor was installed outside the metal box to drive the instrument to rotate in the vertical direction for observation at different elevation angles [19]. In this study, each sequence contained 9 elevation angles ($0°$, $1°$, $2°$, $3°$, $6°$, $10°$, $20°$, $30°$, and $90°$), and it took about 4 min for a complete sequence. The spectrograph covered the wavelength range of 290–447 nm. A temperature control module was used to ensure that the spectrograph was operating at stable temperature lower than the ambient temperature. Solar scattering spectra were collected during the daytime period. The spectra of dark current and electron offset were also measured at specific operating temperatures, which were used to correct the measured spectra in the daytime and then reduce the influence of the spectrograph's photoelectric noise [32]. More information about the instrumentation parameters can be found in the previous studies [31,43,44].

*2.2. Spectral Analysis*

According to the Beer–Lambert law, the differential slant column density (dSCD) can be retrieved from the measured scattering spectra by the DOAS method [19]. The dSCDs are the differences in slant column densities between the measured and reference spectra. The spectral analysis procedure was implemented by QDOAS software [45]. Before the spectral analysis, the spectra during the observation period were divided into 9 segments based on the operating temperature of the spectrograph. The observed spectra within each segment are corrected by using their corresponding spectra of dark current and electron offset. The high-resolution solar spectral were used for the wavelength calibration. $NO_2$ and HCHO dSCDs were retrieved in wavelength ranges of 351~390 nm and 324~359 nm, respectively.

The fitting parameters for $NO_2$ and HCHO spectral analyses were similar as in previous studies [36,45,46], see Table 1. In this study, in order to improve the credibility of the data, only the spectra with root mean square (RMS) of the spectral fitting residuals < 0.003 and solar zenith angle (SZA) < 75° were retained [46,47]. Under the control of these two thresholds, we retained 70.67% of the $NO_2$ profiles and 68.77% of the HCHO profiles. Figure 2 shows an example of spectral fitting for $NO_2$ and HCHO dSCDs from the spectrum measured at 10:00 Beijing time (BJ, UTC + 8 h) on 5 July 2021 at an elevation angle of 10°.

**Table 1.** Setting for $NO_2$ and HCHO spectral analyses.

| Parameters | $O_4$ and $NO_2$ | HCHO |
|---|---|---|
| Fraunhofer reference | sequential spectra | |
| Fitting interval | 351~390 nm | 324~359 nm |
| DOAS polynomial | degree: 5 | |
| Intensity offset | degree: 2 (constant and order 1) | |
| Shift and stretch | spectral | |
| Ring spectra | Original and wavelength-dependent Ring spectra | |
| $NO_2$ cross section | Vandaele et al. (1998) [48], 294 K, 220 K, $I_0$ correction ($10^{17}$ molecule·cm$^{-2}$) | Vandaele et al. (1998) [48], 294 K, $I_0$ correction ($10^{17}$ molecule·cm$^{-2}$) |
| $O_3$ cross section | Serdyuchenko et al. (2014) [49], 223 K, $I_0$ correction ($10^{20}$ molecule·cm$^{-2}$) | Serdyuchenko et al. (2014) [49], 223 K, 243 K, $I_0$ correction ($10^{20}$ molecule·cm$^{-2}$) |
| $O_4$ cross section | Thalman and Volkamer (2013) [50], 293 K | |
| HCHO cross section | Meller and moortgat (2000) [51], 298 K | |
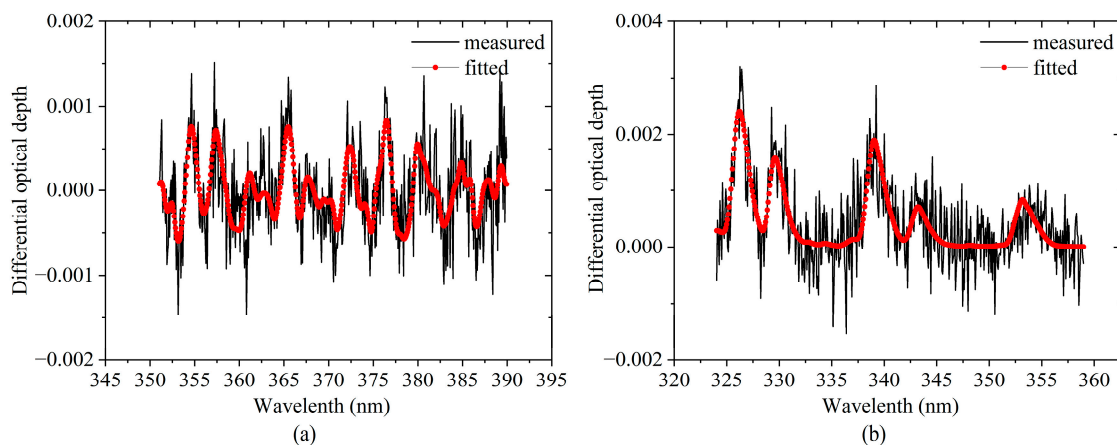


**Figure 2.** Examples of spectral fitting for (**a**) $NO_2$ and (**b**) HCHO. Black and red curves are the measured and fitted differential optical depths, respectively. The $NO_2$ and HCHO dSCDs are $1.10 \times 10^{16}$ molecule·cm$^{-2}$ and $2.30 \times 10^{16}$ molecule·cm$^{-2}$, respectively. The RMS between measured and fitted spectra are $7.63 \times 10^{-4}$ for $NO_2$ and $8.98 \times 10^{-4}$ for HCHO, respectively.

## 2.3. Retrieval of $NO_2$ and HCHO Vertical Profiles

The vertical profiles of $NO_2$ and HCHO VMRs in the lower troposphere (0~4 km) were retrieved from the dSCDs by using the Profile inversion algorithm of aerosol extinction and the trace gas concentration algorithm (PriAM) [47]. The inversion consists of two procedures. In the first step, the vertical profiles of aerosol extinction (AE) were retrieved from the measured $O_4$ dSCDs. Then the retrieved AE profiles were used for the inversion

of the trace gas profiles [45,47]. For HCHO, the AE profiles at 360 nm were transformed into profiles at 343 nm by using the Ångström exponent. In this study, we set the Ångström exponent as 0.7, which was estimated based on the ERA5 reanalysis data. The entire observation period was divided into six segments according to the working temperature of the spectrograph. The inversion parameters of surface albedo, single scattering albedo, and asymmetry factor were listed in Table 2.

**Table 2.** Surface albedo, single scattering albedo, and asymmetry factor for each segment of profile inversion.

| NO. | Start and End Time | Surface Albedo | Single Scattering Albedo | Asymmetry Factor |
|---|---|---|---|---|
| 1 | 2020/10/26—2020/11/18 | 0.11 | 0.94 | 0.7 |
| 2 | 2020/11/19—2020/12/08 | 0.22 | 0.94 | 0.7 |
| 3 | 2021/03/04—2021/04/07 | 0.13 | 0.93 | 0.7 |
| 4 | 2021/04/07—2021/06/12 | 0.15 | 0.92 | 0.7 |
| 5 | 2021/06/13—2021/07/27 | 0.17 | 0.94 | 0.7 |
| 6 | 2021/08/01—2021/10/12 | 0.15 | 0.96 | 0.7 |

The PriAM algorithm was based on the optimal estimation method to obtain the vertical profiles via loop iteration, which minimized the parameter of cost function [47,52]. The smaller values of the cost function correspond to the more reliable retrieval results. The relative deviations of dSCDs reflect the differences between the PriAM and MAX-DOAS measurements. In order to balance the data quality and quantity, we retained the profiles with cost function < 30 and dSCDs relative deviations < 45% during the post-processing. With respect to the selected thresholds, 61.72% of $NO_2$ profiles and 51.71% of HCHO profiles were left.

*2.4. Ancillary Datasets*

The in situ $NO_2$ concentration and meteorological data such as surface temperature, relative humidity, and wind speed used in this study were derived from synchronous operational observations at the LFS station. Surface temperature, relative humidity, and wind speed were measured using an automatic meteorological station (DZZ5, Huayun Sonding, China), with precisions of $\pm$ 0.1 °C, $\pm$ 1%, and $\pm$ 0.1 m/s, respectively. The meteorological measurements follow the standard (QX/T 61−2007). The Ångström exponent, surface albedo, planetary boundary layer height (PBLH), and temperature–pressure a priori profiles were obtained from ERA5 reanalysis data (https://www.ecmwf.int/en/forecasts/dataset/ecmwf-reanalysis-v5, accessed on 25 May 2021). The asymmetry factor, single scattering albedo, and Ångström exponent were also referred to the data from the Aerosol Robotic Network (AERONET, https://aeronet.gsfc.nasa.gov/, accessed on 26 May 2021). The instrument used in the AERONET network was the CE318 multi−wavelength solar photometer (CIMEL, Paris, France).

**3. Results**

*3.1. Overview*

The averaged $NO_2$ and HCHO vertical profiles below 4 km for the whole observation period are shown by the lines with dots in Figure 3. The $NO_2$ VMR has the largest value at the surface and decreases with increasing altitude. There is an elevated HCHO pollution layer with VMRs larger than 2 ppb around the altitudes of 1.4 km. The means $\pm$ standard deviations of $NO_2$ and HCHO VCDs are $4.69 \pm 3.72 \times 10^{15}$ and $1.19 \pm 0.84 \times 10^{16}$ molecule·cm$^{-2}$, respectively. Correspondingly, the near-surface VMRs are $1.22 \pm 1.09$ ppb for $NO_2$ and $2.41 \pm 3.26$ ppb for HCHO. The near-surface VMRs of $NO_2$ and HCHO in this study are higher than those of $NO_2$ (7~100 ppt) and HCHO (0.9 ppb) at the Waliguan regional atmospheric background station from 2012 to 2015 [36].
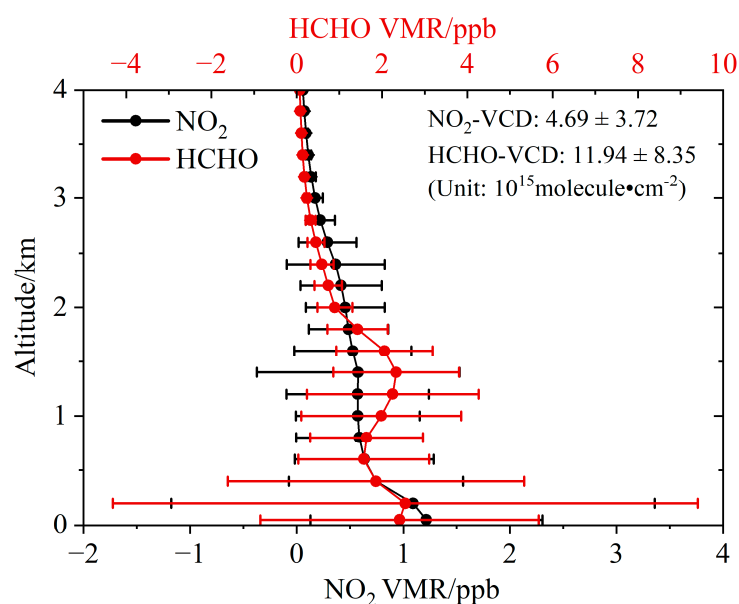
**Figure 3.** Vertical profiles of $NO_2$ (black) and HCHO (red) VMRs. The lines with dots and the error bars indicate the means and standard deviations at different altitudes during the observation period. The averaged values $\pm$ standard deviations of tropospheric $NO_2$ and HCHO VCDs (Unit: $10^{15}$ molecule·cm$^{-2}$) during the observation period are also shown in the figure.

### 3.2. Temporal Variations

#### 3.2.1. Monthly Variations

The monthly variations of the vertical profiles were different between $NO_2$ and HCHO (Figure 4). The larger $NO_2$ VMRs occur at the near-surface and decrease with increasing altitudes each month. The $NO_2$ VMRs were lower in the lower troposphere in summer than in other seasons. For HCHO, larger VMRs appear not only near the surface but also at upper levels (~1.4 km altitude) in most observational months.
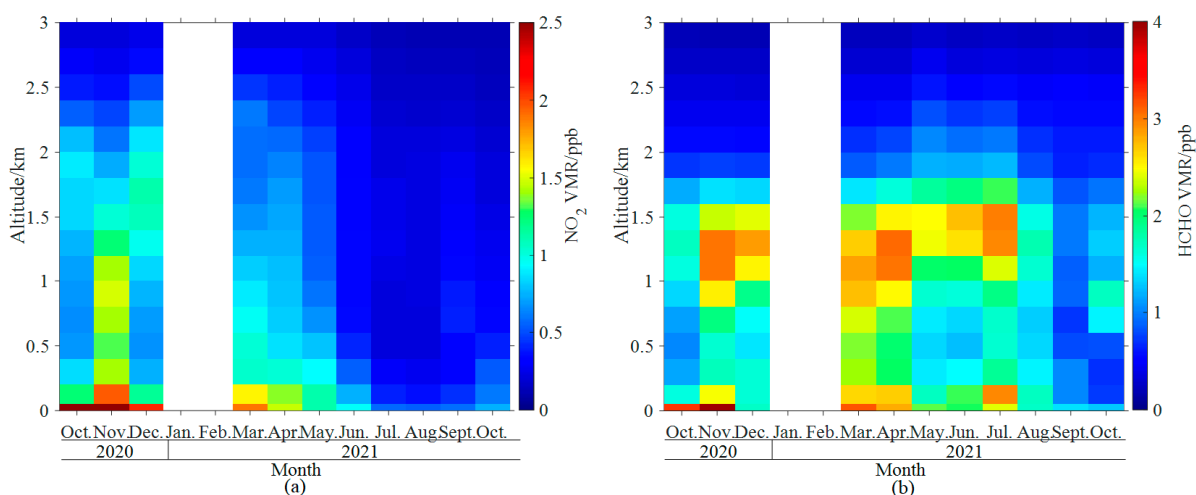


**Figure 4.** Monthly vertical profiles of (**a**) $NO_2$ and (**b**) HCHO VMRs.

The maxima (minimum) of monthly averaged $NO_2$ near-surface VMRs (Figure 4a) and VCDs (Figure 5a) were 2.51 ppb (0.47 ppb) and $8.6 \times 10^{15}$ molecule·cm$^{-2}$ ($2.00 \times 10^{15}$ molecule·cm$^{-2}$) in November 2020 (August 2021). Tropospheric $NO_2$ VCD shows a monthly variation trend of being higher in colder months and lower in warmer months (Figure 5a). The open burning of straw in autumn and the burning of fuel for heating in winter probably lead to an increase in $NO_2$ emissions compared to summer.

The cold and dry atmospheric conditions in autumn and winter are not conducive to gas spreading, resulting in the highest $NO_2$ concentrations in autumn and winter [53].
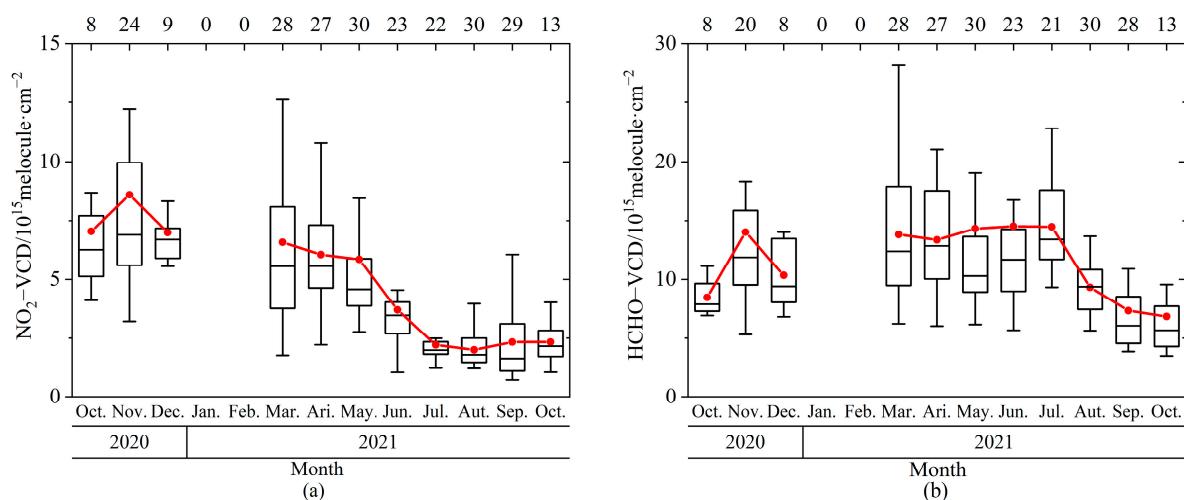


**Figure 5.** Monthly tropospheric VCDs (Unit: $10^{15}$ molecule·cm$^{-2}$) for (**a**) $NO_2$ and (**b**) HCHO. The upper (lower) error bars and upper (lower) boundaries of the boxes are the 95th (5th) and 75th (25th) percentiles of the data grouped per month, respectively. The lines inside the boxes and the red curves with dots indicate the medians and the averages, respectively. The number of sampling days per month is marked on the top axis.

The monthly HCHO VCDs maintained a high level from March to July 2021, with a maximum of $1.45 \times 10^{16}$ molecule·cm$^{-2}$ in June (Figure 5b). The HCHO minimum for both near-surface VMRs (1.12 ppb, Figure 4b) and VCDs ($6.83 \times 10^{15}$ molecule·cm$^{-2}$, Figure 5b) appeared in October 2021. The near-surface HCHO VMRs were enhanced from late October to early December 2020, probably due to increased primary HCHO emissions from fossil fuel combustion in North China during the heating period [54]. The HCHO vertical distribution and column were influenced by complex factors, such as primary source from fossil fuel combustion [8] and secondary sources from chemical oxidation reactions [9]. The causes of HCHO temporal variation should be further investigated by comprehensive observation in future.
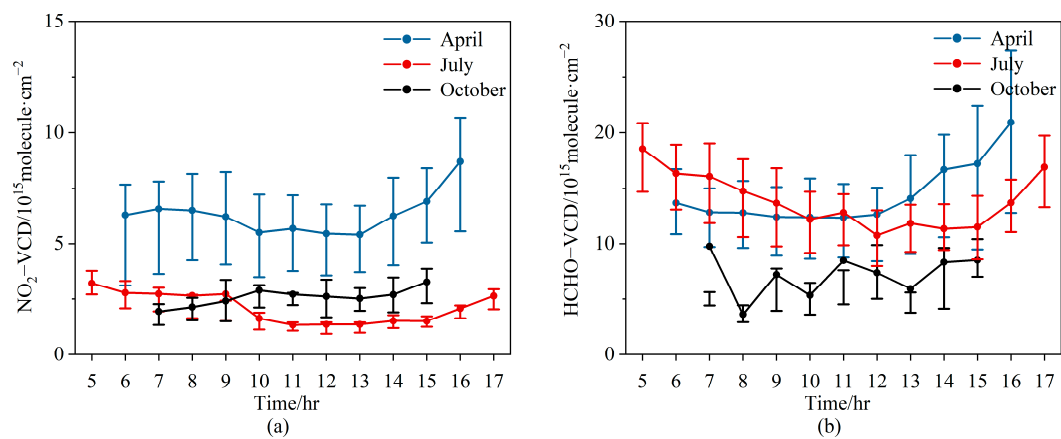
3.2.2. Diurnal Variations

In this study, we use April, July, and October 2021 as representatives of spring, summer, and autumn, respectively. The sample number in winter was too small to be discussed here. Figure 6 shows the diurnal variations of the vertical profile of $NO_2$ and HCHO VMRs in April, July, and October 2021. High near-surface $NO_2$ VMRs occurred in the early morning (5:00–9:00 BJ) and late evening (15:00–17:00 BJ) during April and July, but were stable throughout the daytime in October. In all three months, a polluted layer of $NO_2$ was present in the residual layer. The planetary boundary layer developed to a maximum at 13:00 BJ. The elevated layer of $NO_2$ disappeared gradually as the planetary boundary layer developed. The elevated layer existed throughout the day. Active photochemical reactions in the upper planetary boundary layer can contribute to the persistence of the HCHO elevation layer in the afternoon [55]. This characteristic is consistent with our observations at Raoyang meteorological station [46].
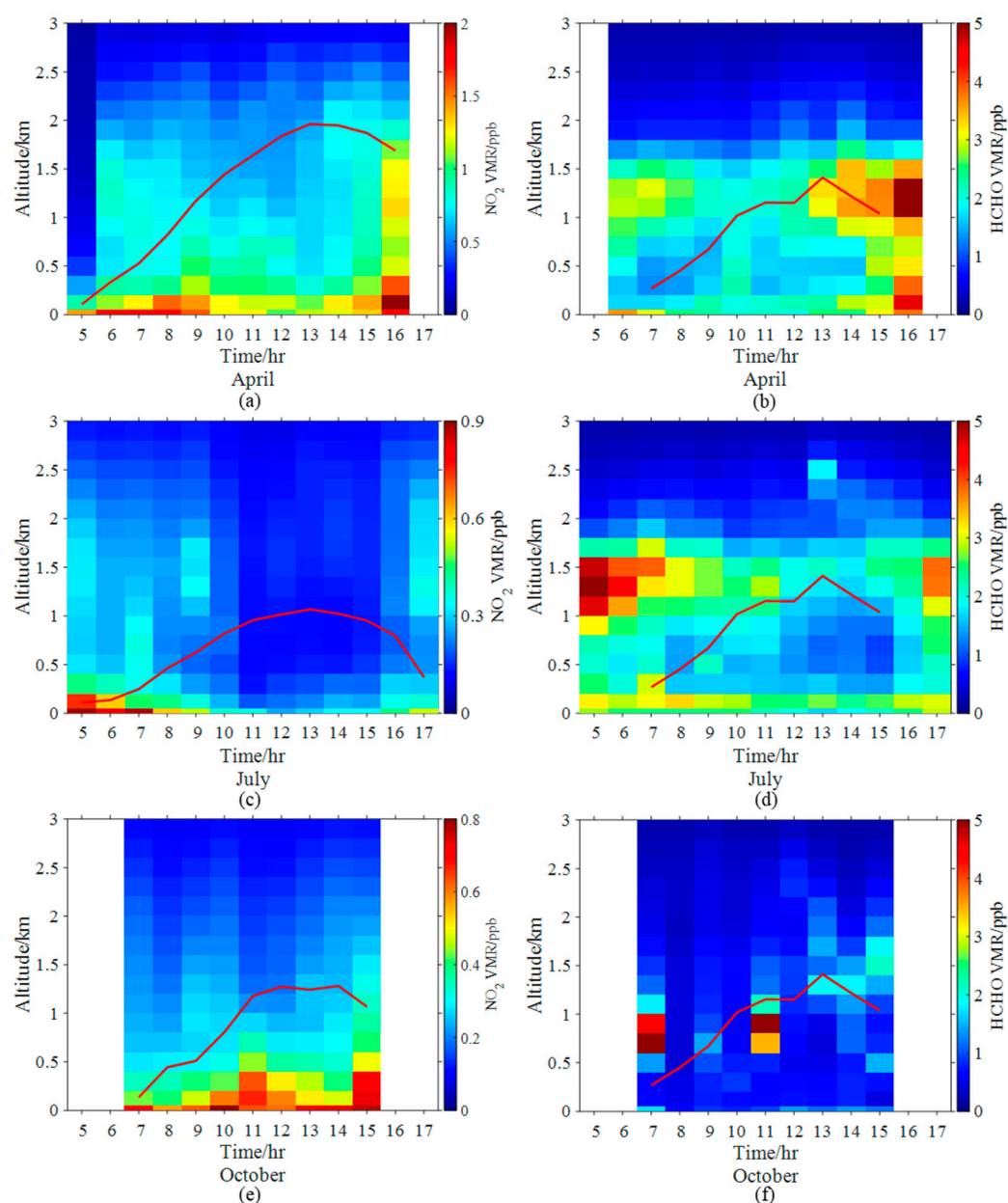
**Figure 6.** Diurnal variations of the vertical profile of $NO_2$ in April (**a**), July (**c**) and October (**e**). (**b**,**d**,**f**) Same as (**a**,**c**,**e**) correspondingly, but for HCHO. The red line indicates the planetary boundary layer height (PBLH).

The daily variations of $NO_2$ and HCHO VCDs are shown in Figure 7. $NO_2$ VCDs remained at almost the same level throughout the day in April, with a slight increase after 14:00 BJ. In July, $NO_2$ VCDs slightly decreased from 5:00 to 9:00 BJ, stayed almost the same from 10:00 to 15:00 BJ, and then increased slightly after 16:00 BJ. In October, $NO_2$ VCDs were nearly constant throughout the day. The $NO_2$ diurnal patterns were different from those in urban areas, where there are two peaks in the morning and evening due to traffic emissions [56]. For all three months, the $NO_2$ diurnal variations ranges were small, implying that the local anthropogenic emission and photochemical reactions were weak at the LFS background station.

**Figure 7.** Diurnal variations of tropospheric VCDs for (**a**) NO₂ and (**b**) HCHO. The dots denote the averages, and the error bars represent the 25th and 75th percentiles of the data grouped for each hour. The blue, red, and black dotted lines denote April, July and October 2021, respectively.

In April, HCHO VCDs varied gently during the period from 06:00 to 12:00 BJ and started to increase at 12:00 BJ until they reached the highest value at 16:00 BJ. In July, HCHO concentrations were high in the morning and evening but low at noon, with the maximum value appearing at 05:00 BJ. HCHO VCDs decreased to a minimum at 12:00 BJ and remained stable until 15:00 BJ. By comparing with the corresponding temperature and relative humidity qualitatively (Figure 8), we found that high NO₂ VCDs tended to occur at low temperatures and high humidity, but this relationship was not found between HCHO and temperature. Because of the low wind speeds, the LFS station was mainly influenced by emissions from local sources.
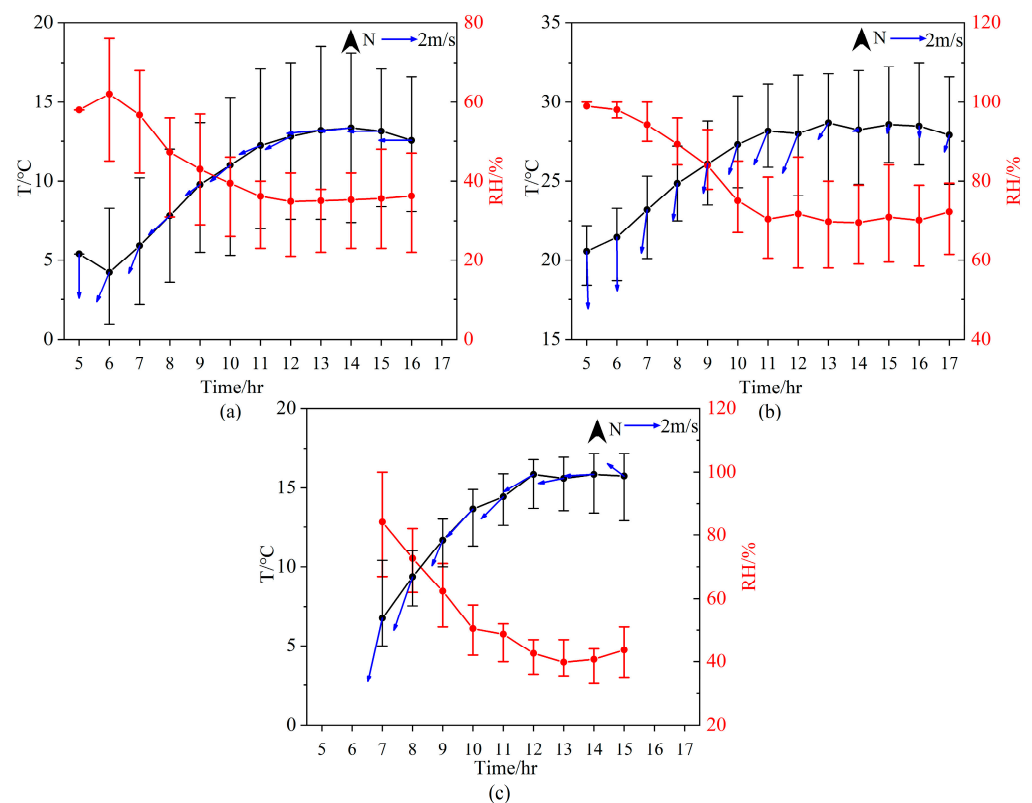


**Figure 8.** Diurnal variations of temperature (black), relative humidity (red), wind speed and direction (blue) in (**a**) April, (**b**) July and (**c**) October 2021.

### *3.3. HCHO/NO$_2$ Ratio*

#### 3.3.1. Temporal Variation

The production of tropospheric ozone (O$_3$) in most regions is associated with VOCs and NO$_x$ [57]. The ratio of HCHO to NO$_2$ is an effective indicator for investigating the sensitivity of chemical ozone production to nitrogen oxides (NO$_x$) and VOCs [46,58,59]. "RA" is used to refer to the ratio of HCHO to NO$_2$, either in VMRs (RA$_{VMR}$) or tropospheric VCD (RA$_{VCD}$). According to previous studies, O$_3$ production can be divided into VOCs-limited (RA < 1), transition zone (1 < RA < 2) and NO$_x$-limited (RA > 2) [60,61]. In this study, in order to balance the quality and quantity of the data, only HCHO VMRs between 1 and 10 ppb and NO$_2$ larger than 0.1 ppb were considered for the calculation of RA [46].

RA with respect to VMR has an elevated layer at the altitude of around 1.5 km (Figure 9a). The vertical distribution of the monthly means of RA (Figure 9b) shows that the height of the lower boundary of the elevated RA fell from October 2020 (1.2 km) to May 2021 (0.8 km). The larger RA filled the entire lower troposphere (below 2 km) from June until September 2021. In October 2021, RA in the lower troposphere decreased, and the lower boundary of the elevated layer rose again to 1.2 km. The majority of RA were less than 2 above the altitude of 2 km and less than 1 above the altitude of 2.5 km. The RAs of near-surface VMR and tropospheric VCD had the same seasonal variation patterns, with annual averages of 2.97 ± 3.04 for near-surface VMR and 4.03 ± 3.63 for tropospheric VCD (Figure 9c). The largest values of both RA$_{VMR}$ and RA$_{VCD}$ appeared in July, being 6.25 ± 4.00 and 8.22 ± 3.62, respectively. Correspondingly, the lowest RA appeared in December with the values of 0.96 ± 0.36 for RA$_{VMR}$ and 1.53 ± 0.67 for RA$_{VCD}$.
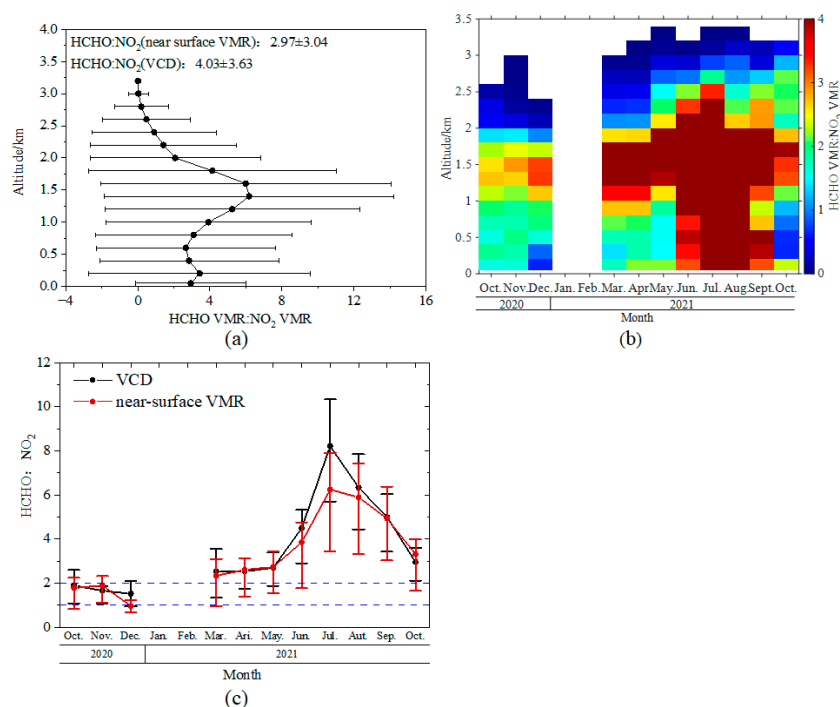


**Figure 9.** (**a**) Vertical profiles of the ratio of HCHO to NO$_2$ during the observation period. The dots and whiskers indicate the average of all data at selected altitudes during the observation period and the standard deviation, respectively. (**b**) Monthly variation of vertical profiles of VMRs ratios of HCHO to NO$_2$. (**c**) Monthly variation of the ratio of HCHO to NO$_2$ for tropospheric VCDs and near-surface VMRs. The dots and the error bars denote the averages and the 25th and 75th percentiles of the data grouped for each month. HCHO/NO$_2$ = 1 and 2 are also marked with dashed lines. The white grid cells in panel (**b**) indicate the missing data owing to lacking observation and data quality control.

The diurnal variation patterns of RA vertical distribution varied with seasons (Figure 10). In each month, the elevated layer of RA appeared around the altitudes of 1.5 km. In April, the RA was mainly between 1 and 2 in the lower boundary layer (0–0.4 km), with RA < 1 above 2.5 km. In July, RA > 2 filled the entire boundary layer (up to 2 km), with RA < 2 only appearing above 2 km. In October, RA was almost between one and two near the surface. The $RA_{VCD}$ was larger than two in all the three months. On average, the RA in July was ~3.2 and ~2.8 times higher than that in April and October, respectively.
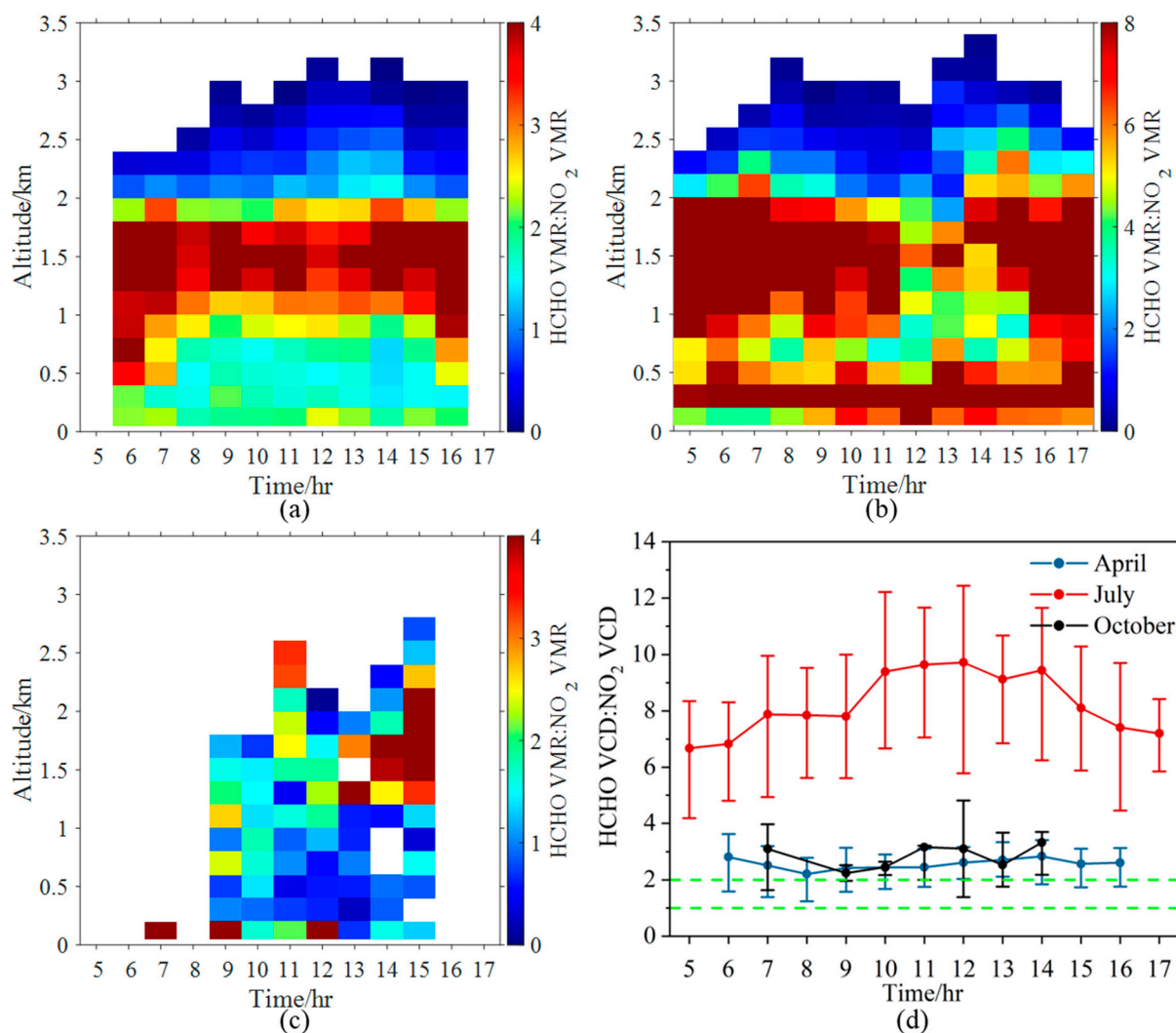


**Figure 10.** Diurnal variations in the vertical profile of the ratio of HCHO to $NO_2$ VMRs in (**a**) April, (**b**) July, and (**c**) October 2021. (**d**) Diurnal variations of $RA_{VCD}$ in April, July, and October 2021. The dots and error bars represent the averages and the 25th (75th) percentiles of the data grouped for each hour in April (blue), July (red) and October (black).

### 3.3.2. Implication for $O_3$ Production

To analyze the sensitivities of $O_3$ production to the ratio of HCHO to $NO_2$, we assume that daily $O_3$ production at the LFS is approximately equal to the range of daytime $O_3$ concentration variations at the surface, considering that the photochemical $O_3$ production was a strong driver of the diurnal surface $O_3$ variation [46,59]. Figure 11 shows the daily $O_3$ production as a function of the daily average values of HCHO and $NO_2$ for near-surface VMR (Figure 9a) and VCD (Figure 9b) during the daytime (05:00 to 17:00 BJ). The distribution patterns of $O_3$ production, as classified by $RA_{VMR}$ and $RA_{VCD}$, are similar. For most of the days, $O_3$ production was concentrated in the $NO_x$-limited regions or transition

regions. On only a few days was the weaker $O_3$ production (<20 ppb d$^{-1}$) located in the VOCs-limited regions. Differently, the strongest near-surface $O_3$ production occurred in the transition region for RA$_{VMR}$, but in the NO$_x$-limited region for RA$_{VCD}$. From October 2020 to March 2021, the RA$_{VMR}$ varied between 1 and 2, implying that $O_3$ production was in the transition regime. As a whole, $O_3$ production was in the NO$_x$-limited regime.
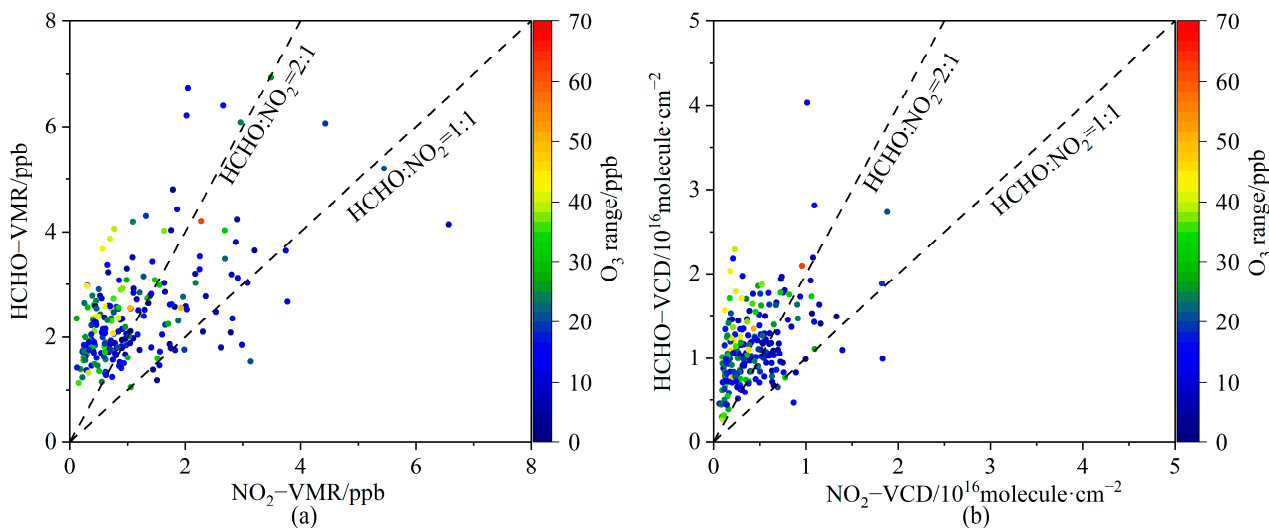


**Figure 11.** (**a**) Daily average of near-surface VMRs for HCHO and NO$_2$. (**b**) same as (**a**) but for VCDs, colored by the range of daytime surface $O_3$ variation. The dashed lines indicate HCHO/NO$_2$ = 1 and 2.

### 3.3.3. Relationship to Meteorological Conditions

The correlation coefficient between RA$_{VMR}$ and temperature (relative humidity) is 0.62 (0.53), implying that $O_3$ production at LFS tended to be in the NOx−limited region when the temperature and relative humidity were higher (Figure 12a, b). In July, the temperature and relative humidity were high, and the RA was basically larger than two. There is no correlation relationship between RA$_{VMR}$ and wind speed (Figure 12c), with the correlation coefficient of 0.01 (not shown in figure). However, the RA$_{VMR}$ is dependent on the wind directions (Figure 12d–f). In April, maximum frequencies for RA$_{VMR} \geq 2$ and $1 < $ RA$_{VMR} < 2$ were 14.81% in the SSW sector and 11.11% in the NNW sectors. Almost all the RA$_{VMR}$ values in July were larger than two and distributed in the SE–WSW sectors, with the largest frequency occurring in the S direction. In October, the largest frequency for RA$_{VMR} > 2$ was 33.33% in the SSW direction and the frequencies for $1 < $ RA$_{VMR} < 2$ were smaller and in the N and ESE directions. As a whole, the sensitivity of $O_3$ production to NO$_2$ and HCHO is closely related to temperature and relative humidity. Air masses from different directions can lead to different sensitivities of $O_3$ production to NO$_x$ and VOCs at LFS Station.
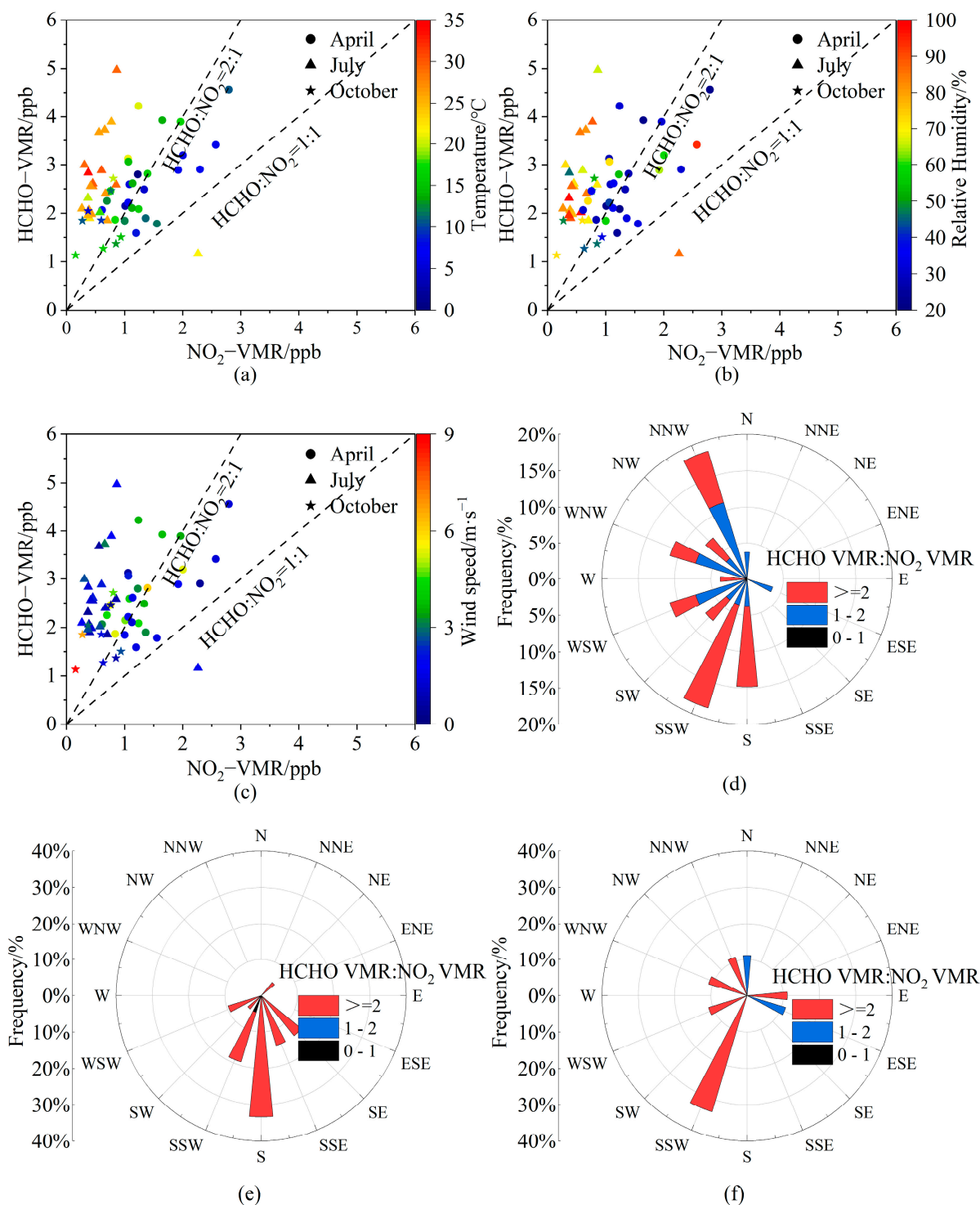
**Figure 12.** Relationship between the near-surface VMR ratios of HCHO to NO$_2$ and meteorological factors, i.e., (**a**) air temperature, (**b**) relative humidity, (**c**) wind speed, and (**d**−**f**) wind direction. The dots, triangles, and pentagrams represent April, July, and October 2021, respectively. Rose plots denote RA$_{VMR}$ frequencies in 16 wind directions in (**d**) April, (**e**) July and (**f**) October 2021.

## 4. Discussion

The averaged NO$_2$ VCDs (4.69 × 10$^{15}$ molecule·cm$^{-2}$) during our observation period are larger than the mean level (1.16 × 10$^{15}$ molecule·cm$^{-2}$) in Heilongjiang province from 2005 to 2015 [60]. However, the mean HCHO VCDs in this study (1.19 × 10$^{16}$ molecule·cm$^{-2}$) are lower than those (1.39 × 10$^{16}$ molecule·cm$^{-2}$) in Heilongjiang province from 2005 to 2018 [61].

The background levels of $NO_2$ and HCHO at LFS are useful to investigate as long-term trends in future studies.

The ranges of diurnal variation of $NO_2$ VCDs are smaller at the LFS station than at another WMO/GAW background region in the North China Plain [35]. The vertical profile structures of both $NO_2$ and HCHO at LFS in summer are similar to those observed at Raoyang, a rural site in the North China Plain [46]. The MAX−DOAS measurements at Raoyang were performed only for a summer period, and the elevated HCHO layer can be attributed to the air pollution and oxidization process in the lower atmosphere in the North China Plain [55]. The causes of larger VMRs at upper levels (~1.4 km altitude) at the LFS background station need to be fully understood in future studies.

Meteorological conditions affected the concentration levels, vertical distribution, and temporal variations of $NO_2$ and HCHO, as well as the sensitivity of $O_3$ production at the LFS station. There are at least three reasons: (1) The boundary layer evolution led to the vertical mixing of air masses; (2) The temperature and relative humidity affected the efficiency of $O_3$ photochemical processes and the natural source emission; (3) Different wind speeds and directions were accompanied by air masses with different pollution levels.

## 5. Conclusions

We carried out MAX−DOAS observations at the Longfengshan regional atmospheric background station in Heilongjiang Province of China from October 2020 to October 2021, performed the spectral analysis with QDOAS software, and retrieved vertical profiles of $NO_2$ and HCHO by using the PriAM algorithm. We explored the concentration, temporal, and spatial variation of $NO_2$ and HCHO, and the sensitivity of $O_3$ production to the ratio of HCHO to $NO_2$. The conclusions are as follows:

The average levels of near-surface VMRs for $NO_2$ and HCHO were $1.22 \pm 1.09$ ppb and $2.41 \pm 3.26$ ppb throughout the observation period, respectively. The $NO_2$ vertical structure shows a declining pattern with increasing altitude, while HCHO has an elevated layer around the altitude of 1.4 km.

The $NO_2$ VMRs in the lower troposphere tend to be higher in colder months and lower in warmer months at the LFS station. HCHO has an opposite monthly trend, especially at upper levels (~1.4 km altitude). There was a polluted layer of $NO_2$ in the residual layer, which disappeared gradually with the development of planetary boundary layer. However, the HCHO elevated layer maintained throughout the daytime. Different from the gentle diurnal variations of $NO_2$ VCDs, the HCHO VCDs are high in the morning and evening but low at noon in July. The qualitative comparisons show that high $NO_2$ VCDs tended to occur at low temperatures and high humidity, but this relationship is not found for HCHO.

Although there were monthly and diurnal variations in the vertical profiles of the VMR ratio of HCHO to $NO_2$, on most of the days, $O_3$ production was in the $NO_x$-limited regions or transition regions at the LFS station. There were only a few days of the experiment time when the weaker $O_3$ production (<20 ppb) was located in the VOCs-limited regions. Besides the dependencies of wind direction, the $O_3$ production at the LFS tended to be in the NOx-limited region when the temperature and relative humidity were higher.

The results of this study will be helpful for better understanding the spatiotemporal distribution characteristics of $NO_2$ and HCHO in the background region, in addition, more comprehensive observations, such as concurrent measurements of $O_3$ and VOCs together with MAX-DOAS, are recommended, which are significant for evaluating and designing the strategies for controlling $O_3$ pollution.

**Author Contributions:** Conceptualization, S.L., S.C., J.M. and X.X.; methodology, S.L., S.C. and J.M.; validation, X.X., X.D. and D.Y.; formal analysis, S.L., S.C. and J.M.; investigation, S.L., J.G., J.L. and J.J.; resources, X.X. and J.M.; data curation, S.L., S.C. and J.M.; writing—original draft preparation, S.L.; writing—review and editing, S.L., S.C., J.M. and X.X.; visualization, S.L.; supervision, J.M.; project

## References

1. Seinfeld, J.H.; Pandis, S.N. *Atmospheric Chemistry and Physics: From Air Pollution to Climate Change*, 2nd ed.; John Wiley & Sons, Inc.: Hoboken, NJ, USA, 2006.
2. Logan, J.A. Nitrogen oxides in the troposphere: Global and regional budgets. *J. Geophys. Res.* **1983**, *88*, 10785–10807. [CrossRef]
3. Luo, C.; Zhou, X. The Study of The Cycle of Nitrogen Oxides in The Troposphere. *Q. J. Appl. Meteorol.* **1993**, *4*, 92–99.
4. Brimblecombe, P.; Chu, M.; Liu, C.-H.; Fu, Y.; Wei, P.; Ning, Z. Roadside $NO_2/NO_x$ and primary $NO_2$ from individual vehicles. *Atmos. Environ.* **2023**, *295*, 119562. [CrossRef]
5. Bauwens, M.; Compernolle, S.; Stavrakou, T.; Müller, J.F.; Gent, J.; Eskes, H.; Levelt, P.F.; Van Der A, R.; Veefkind, J.P.; Vlietinck, J.; et al. Impact of Coronavirus Outbreak on $NO_2$ Pollution Assessed Using TROPOMI and OMI Observation. *Geophys. Res. Lett.* **2020**, *47*, e2020GL087978. [CrossRef] [PubMed]
6. Labzovskii, L.D.; Belikov, D.A.; Damiani, A. Spaceborne $NO_2$ observations are sensitive to coal mining and processing in the largest coal basin of Russia. *Sci. Rep.* **2022**, *12*, 12597. [CrossRef] [PubMed]
7. Agency, E. *Nitrogen Oxides (NOx), Why and How They Are Controlled*; DIANE Publishing: Collingdale, PA, USA, 1999.
8. Peng, W.; Wang, Y.; Gao, X.; Jia, S.; Xu, X.; Cheng, H.; Meng, Z. Characteristics of Ambient Formaldehyde at Two Rural Sites in the North China Plain in Summer. *Res. Environ. Sci.* **2016**, *29*, 1119–1127. [CrossRef]
9. Wang, S.; Wang, H.; Liu, B. Determination of Atmospheric Formaldehyde in Beijing by High-Performance Liquid Chromatography. *Res. Environ. Sci.* **2008**, *21*, 27–30. [CrossRef]
10. Parrish, D.D.; Ryerson, T.B.; Mellqvist, J.; Johansson, J.; Herndon, S.C. Primary and secondary sources of formaldehyde in urban atmospheres: Houston Texas region. *Atmos. Chem. Phys.* **2012**, *12*, 3273–3288. [CrossRef]
11. Kaiser, J.; Jacob, D.J.; Lei, Z.; Travis, K.R.; Fisher, J.A.; Abad, G.G.; Lin, Z.; Zhang, X.; Fried, A.; Crounse, J.D. High-resolution inversion of OMI formaldehyde columns to quantify isoprene emission on ecosystem-relevant scales: Application to the southeast US. *Atmos. Chem. Phys.* **2018**, *18*, 5483–5497. [CrossRef]
12. Jin, X.; Fiore, A.; Boersma, K.F.; Smedt, I.D.; Valin, L. Inferring Changes in Summertime Surface Ozone-$NO_x$-VOC Chemistry over U.S. Urban Areas from Two Decades of Satellite and Ground-Based Observations. *Environ. Sci. Technol.* **2020**, *54*, 6518–6529. [CrossRef]
13. Tan, Z.; Lu, K.; Jiang, M.; Su, R.; Dong, H.; Zeng, L.; Xie, S.; Tan, Q.; Zhang, Y. Exploring ozone pollution in Chengdu, southwestern China: A case study from radical chemistry to $O_3$-VOC-$NO_x$ sensitivity. *Sci. Total Environ.* **2018**, *636*, 775–786. [CrossRef]
14. Zhang, Y.; Li, Z.; Zhao, S.; Zhang, X.; Lin, J.; Qin, K.; Liu, C.; Zhang, Y. A review of collaborative remote sensing observation of atmospheric gaseous and particulate pollution with atmospheric environment satellites. *Natl. Remote Sens. Bull.* **2022**, *5*, 873–896.
15. Cheng, S.; Cheng, X.; Ma, J.; Xu, X.; Zhang, W.; Lv, J.; Bai, G.; Chen, B.; Ma, S.; Dörner, S.; et al. Mobile MAX-DOAS observations of tropospheric NO2 and HCHO during summer over the Three Rivers' Source region in China. *Atmos. Chem. Phys. Discuss.* **2022**, 1–36. [CrossRef]
16. Zhang, X.; Song, Q.; Gao, Y.; Wang, P.; Yu, D.; Wang, M.; Wen, M. Domestic in-situ Analyzer of Greenhouse Gases with Fourier Transform Infrared Spectroscopy and its Primary Application in Atmospheric Background Observation. *J. Atmos. Environ. Opt.* **2019**, *14*, 279–288. [CrossRef]
17. Xu, J.; Xie, P.; Si, F.; Dou, K.; Li, A.; Liu, Y.; Liu, W. Retrieval of Tropospheric $NO_2$ by Multi Axis Differential Optical Absorption Spectroscopy. *Spectrosc. Spectr. Anal.* **2010**, *30*, 2464–2469. [CrossRef]
18. Wagner, T.; Dix, B.; Friedeburg, C.v.; Frieß, U.; Sanghavi, S.; Sinreich, R.; Platt, U. MAX-DOAS $O_4$ measurements: A new technique to derive information on atmospheric aerosols—Principles and information content. *J. Geophys. Res.* **2004**, *109*, D22205. [CrossRef]
19. Hönninger, G.; von Friedeburg, C.; Platt, U. Multi axis differential optical absorption spectroscopy (MAX-DOAS). *Atmos. Chem. Phys.* **2004**, *4*, 231–254. [CrossRef]

20. Wittrock, F.; Oetjen, H.; Richter, A.; Fietkau, S.; Burrows, J.P. MAX-DOAS measurements of atmospheric trace gases in Ny-Ålesund-Radiative transfer studies and their application. *Atmos. Chem. Phys.* **2004**, *4*, 955–966. [CrossRef]

21. Friedeburg, C.; Pundt, I.; Mettendorf, K.; Wagner, T.; Platt, U. Multi-axis-DOAS measurements of $NO_2$ during the BAB II motorway emission campaign. *Atmos. Environ.* **2005**, *39*, 977–985. [CrossRef]

22. Ang, L.; PinHua, X.; Cheng, L.; JianGuo, L.; WenQing, L. A Scanning Multi-Axis Differential Optical Absorption Spectroscopy System for Measurement of Tropospheric $NO_2$ in Beijing. *Chin. Phys. Lett.* **2007**, *24*, 2859–2862. [CrossRef]

23. Wang, Y.; Li, A.; Xie, P.-H.; Chen, H.; Mou, F.-S.; Xu, J.; Wu, F.-C.; Zeng, Y.; Liu, J.-G.; Liu, W.-Q. Measuring tropospheric vertical distribution and vertical column density of $NO_2$ by multi-axis differential optical absorption spectroscopy. *Acta Phys. Sin.* **2013**, *62*, 200705. [CrossRef]

24. Jin, J.; Ma, J.; Lin, W.; Zhao, H.; Shaiganfar, R.; Beirle, S.; Wagner, T. MAX-DOAS measurements and satellite validation of tropospheric $NO_2$ and $SO_2$ vertical column densities at a rural site of North China. *Atmos. Environ.* **2016**, *133*, 12–25. [CrossRef]

25. Hendrick, F.; Müller, J.-F.; Clémer, K.; Wang, P.; Mazière, M.D.; Fayt, C.; Gielen, C.; Hermans, C.; Ma, J.Z.; Pinardi, G.; et al. Four years of ground-based MAX-DOAS observations of HONO and NO2 in the Beijing area. *Atmos. Chem. Phys.* **2014**, *14*, 765–781. [CrossRef]

26. Tanvir, A.; Javed, Z.; Jian, Z.; Zhang, S.; Bilal, M.; Xue, R.; Wang, S.; Bin, Z. Ground-Based MAX-DOAS Observations of Tropospheric NO2 and HCHO During COVID-19 Lockdown and Spring Festival Over Shanghai, China. *Remote Sens.* **2021**, *13*, 488. [CrossRef]

27. Xue, J.; Zhao, T.; Luo, Y.; Miao, C.; Su, P.; Liu, F.; Zhang, G.; Qin, S.; Song, Y.; Bu, N.; et al. Identification of ozone sensitivity for NO2 and secondary HCHO based on MAX-DOAS measurements in northeast China. *Environ. Int.* **2022**, *160*, 107048. [CrossRef]

28. Ren, B.; Xie, P.; Xu, J.; Li, A.; Qin, M.; Hu, R.; Zhang, T.; Fan, G.; Tian, X.; Zhu, W.; et al. Vertical characteristics of NO2 and HCHO, and the ozone formation regimes in Hefei, China. *Sci. Total Environ.* **2022**, *823*, 153425. [CrossRef] [PubMed]

29. Luo, Y.; Dou, K.; Fan, G.; Huang, S.; Si, F.; Zhou, H.; Wang, Y.; Pei, C.; Tang, F.; Yang, D. Vertical distributions of tropospheric formaldehyde, nitrogen dioxide, ozone and aerosol in southern China by ground-based MAX-DOAS and LIDAR measurements during PRIDE-GBA 2018 campaign. *Atmos. Environ.* **2020**, *226*, 117384. [CrossRef]

30. Huang, X.; Shao, T.; Zhao, J.; Cao, J.; Song, Y. Spatio-temporal Differentiation of Ozone Concentration and Its DrivingFactors in Yangtze River Delta Urban Agglomeration. *Resour. Environ. Yangtze Basin* **2019**, *28*, 1434–1445. [CrossRef]

31. Ma, J.; Beirle, S.; Jin, J.; Shaiganfar, R.; Yan, P.; Wagner, T. Tropospheric $NO_2$ vertical column densities over Beijing: Results of the first three years of ground-based MAX-DOAS measurements (2008–2011) and satellite validation. *Atmos. Chem. Phys.* **2013**, *13*, 1547–1567. [CrossRef]

32. Jin, J.; Ma, J.; Lin, W.; Zhao, H. Characteristics of $NO_2$ Tropospheric Column Density over a Rural Area in the North China Plain. *J. Appl. Meteorol. Sci.* **2016**, *27*, 303–311. [CrossRef]

33. Li, W.; Ma, J.; Guo, J. Measuring Atmospheric $NO_2$ Column Densities by MAX-DOAS:Method and Application. *Meteorol. Sci. Technol.* **2013**, *41*, 796–802. [CrossRef]

34. Chan, K.; Hartl, A.; Lam, Y.; Xie, P.; Liu, W.; Cheung, H.; Lampel, J.; Poehler, D.; Li, A.; Xu, J. Observations of tropospheric $NO_2$ using ground based MAX-DOAS and OMI measurements during the Shanghai World Expo 2010. *Atmos. Environ.* **2015**, *119*, 45–58. [CrossRef]

35. Cheng, S.; Ma, J.; Zhou, H.; Jin, J.; Liu, Y.; Dong, F.; Zhou, L.; Yan, P. Spectral Inversion and Characteristics of NO_2 Column Density at Shangdianzi Regional Atmospheric Background Station. *Spectrosc. Spectr. Anal.* **2018**, *38*, 3470–3475. [CrossRef]

36. Ma, J.; Steffen, D.; Sebastian, D.; Jin, J.; Cheng, S.; Guo, J.; Zhang, Z.; Wang, J.; Liu, P.; Zhang, G.; et al. MAX-DOAS measurements of $NO_2$, $SO_2$, HCHO, and BrO at the Mt. Waliguan WMO/GAW global baseline station in the Tibetan Plateau. *Atmos. Chem. Phys.* **2020**, *20*, 6973–6990. [CrossRef]

37. Wu, Y.; Ning, S.; Yu, D.; Song, Q.; Dai, X.; Zhao, J. Characteristics of $CO_2$ concentrations and its variations at Longfengshan regional atmospheric background station in Northeast China. *Environ. Chem.* **2015**, *34*, 1627–1632. [CrossRef]

38. Dai, X. Patterns of changes in background values of total ozone at Longfengshan regional background station. *Sci. Technol. Innov. Her.* **2008**, *30*, 177. [CrossRef]

39. Yu, D.; Wu, Y.; Song, Q.; Dai, X.; Lin, W. Environmental Characteristics and Its Observations at Longfengshan WMO Regional Atmospheric Background Station. *Clim. Change Res. Lett.* **2012**, *1*, 65–73. [CrossRef]

40. Xu, X.; Ding, G. Study on acidic gases in the regional background air in northeastern China. *China Env. Ental Sci.* **1997**, *17*, 345–348. [CrossRef]

41. Yu, D.; Song, Q.; Sun, J.; Liu, J.; Wu, Y.; Xia, C. Characteristics of aerosol scattering coefficient at Longfengshan regional background station. *Environ. Chem.* **2019**, *40*, 765–771. [CrossRef]

42. Kreher, K.; Roozendael, M.V.; Hendrick, F.; Apituley, A.; Zhao, X. Intercomparison of $NO_2$, $O_4$, $O_3$ and HCHO slant column measurements by MAX-DOAS and zenith-sky UV-Visible spectrometers during the CINDI-2 campaign. *Atmos. Meas. Tech.* **2020**, *13*, 2169–2208. [CrossRef]

43. Cheng, S.; Jin, J.; Ma, J.; Xu, X.; Ran, L.; Ma, Z.; Chen, J.; Guo, J.; Yang, P.; Wang, Y.; et al. Measuring the Vertical Profiles of Aerosol Extinction in the Lower Troposphere by MAX-DOAS at a Rural Site in the North China Plain. *Atmosphere* **2020**, *11*, 1037–1053. [CrossRef]

44. Cheng, S.; Ma, J.; Cheng, W.; Yan, P.; Zhou, H.; Zhou, L.; Yang, P. Tropospheric $NO_2$ vertical column densities retrieved from ground-based MAX-DOAS measurements at Shangdianzi regional atmospheric background station in China. *J. Environ. Sci.* **2019**, *80*, 186–196. [CrossRef] [PubMed]
45. Platt, U. Differential Optical Absorption Spectroscopy (DOAS). *Air Monit. By Spectrosc. Tech.* **1994**. [CrossRef]
46. Wang, Y.; Dörner, S.; Donner, S.; Böhnke, S.; De Smedt, I.; Dickerson, R.R.; Dong, Z.; He, H.; Li, Z.; Li, Z.; et al. Vertical profiles of $NO_2$, $SO_2$, HONO, HCHO, CHOCHO and aerosols derived from MAX-DOAS measurements at a rural site in the central western North China Plain and their relation to emission sources and effects of regional transport. *Atmos. Chem. Phys.* **2019**, *19*, 5417–5449. [CrossRef]
47. Cheng, S.; Jin, J.; Ma, J.; Lv, J.; Liu, S.; Xu, X. Temporal Variation of $NO_2$ and HCHO Vertical Profiles Derived from MAX-DOAS Observation in Summer at a Rural Site of the North China Plain and Ozone Production in Relation to HCHO/$NO_2$ Ratio. *Atmosphere* **2022**, *13*, 860. [CrossRef]
48. Wang, Y.; Lampel, J.; Xie, P.; Beirle, S.; Li, A.; Wu, D.; Wagner, T. Ground-based MAX-DOAS observations of tropospheric aerosols, $NO_2$, $SO_2$ and HCHO in Wuxi, China, from 2011 to 2014. *Atmos. Chem. Phys.* **2017**, *17*, 2189–2215. [CrossRef]
49. Wang, Y.; Li, A.; Xie, P.H.; Chen, H.; Xu, J.; Wu, F.C.; Liu, J.G.; Liu, W.Q. Retrieving vertical profile of aerosol extinction by multi-axis differential optical absorption spectroscopy. *Acta Phys. Sin.* **2013**, *62*, 180705. [CrossRef]
50. Xiang, X.; Cui, Z.; Zhang, H.; Pei, L.; Chao, M. Analysis of Laws of $NO_2$ Emission and Driving Factors of China's Key Cities. *Environ. Sci. Technol.* **2022**, *045*, 30–45. [CrossRef]
51. Yan, M.; Yang, N.; Zhong, S.; Wang, L. Research on meteorological indicators for heating decisions in Heilongjiang Province. *Heilongjiang Meteorol.* **2021**, *38*, 32–33, 41. [CrossRef]
52. Ma, J.; Wang, Y. The IPAC-NC field campaign: A pollution and oxidization pool in the lower atmosphere over Huabei, China. *Atmos. Chem. Phys.* **2012**, *12*, 3883–3908. [CrossRef]
53. Xu, H.; Liu, H.; Ji, X.; Li, Q.; Liu, G.; Ou, J. Observation of tropospheric $NO_2$ using ground-based MAX-DOAS and OMI measurements during the Shanghai. *Spectrosc. Spectr. Anal.* **2022**, *42*, 2720–2725. [CrossRef]
54. Sillman, S. The relation between ozone, $NO_x$ and hydrocarbons in urban and polluted rural environments. *Atmos. Environ.* **1999**, *33*, 1821–1845. [CrossRef]
55. Ryan, R.G.; Rhodes, S.; Tully, M.; Schofield, R. Surface ozone exceedances in Melbourne, Australia are shown to be under $NO_x$ control, as demonstrated using formaldehyde:$NO_2$ and glyoxal: Formaldehyde ratios. *Sci. Total. Environ.* **2020**, *749*, 141460. [CrossRef] [PubMed]
56. Hong, Q.; Liu, C.; Hu, Q.; Zhang, Y.; Xing, C.; Su, W.; Ji, X.; Xiao, S. Evaluating the feasibility of formaldehyde derived from hyperspectral remote sensing as a proxy for volatile organic compounds. *Atmos. Res.* **2021**, *264*, 105771. [CrossRef]
57. Duncan, B.N.; Yoshida, Y.; Olson, J.R.; Sillman, S.; Martin, R.V.; Lamsal, L.; Hu, Y.; Pickering, K.E.; Retscher, C.; Allen, D.J.; et al. Application of OMI observations to a space-based indicator of NOx and voe controls on surface ozone formation. *Atmos. Environ.* **2010**, *44*, 2213–2223. [CrossRef]
58. Souri, A.H.; Nowlan, C.R.; Wolfe, G.M.; Lamsal, L.N.; Miller, C.E.C.; Abad, G.G.; Janz, S.J.; Fried, A.; Blake, D.R.; Weinheimer, A.J.; et al. Revisiting the effectiveness of HCHO/$NO_2$ ratios for inferring ozone sensitivity to its precursors using high resolution airborne remote sensing observations in a high ozone episode during the KORUS-AQ campaign- ScienceDirect. *Atmos. Environ.* **2020**, *224*, 117341. [CrossRef]
59. Ma, J.; Liu, H. Summertime tropospheric ozone over China simulated with a regional chemical transport model 1. Model description and evaluation. *J. Geophys. Res. Atmos.* **2002**, *107*, ACH 27:21–ACH 27:13. [CrossRef]
60. Zhou, C.; Li, Q.; Zhang, L.; Ma, P.; Chen, H.; Wang, Z. Spatio-tenporal Change and Influencing Factors of Tropospheric $NO_2$ Column Density of China during 2005~2015. *Remote Sens. Technol. Appl.* **2016**, *31*, 1190–1200. [CrossRef]
61. Huang, S.; Li, N.; He, S.; Dong, H. Spatial-temporal Variations and Influencing Factors of Formaldehyde in the Three Provinces of Northeast China during 2005–2018. *Earth Environ.* **2020**, *48*, 652–662. [CrossRef]